Electronic Supplementary Information (ESI)

Data-driven finding of organic anode active materials for lithium-ion battery from natural products of flower scent using capacity predictors

Haruka Tobita,[a] Kosuke Sakano,[a] Hiroaki Imai,[a] Yusuke Yamashita,[b] Yuya Oaki*,[a]

[a] Department of Applied Chemistry, Faculty of Science and Technology, Keio University, 3-14-1 Hiyoshi, Kohoku-ku, Yokohama 223-8522, Japan

[b] R&D Department, Pharma Foods International Co., Ltd., 1-49 Goryo-Ohara, Nishikyo-ku, Kyoto 615-8245, Japan

E-mail: oakiyuya@applc.keio.ac.jp

Experimental methods

Capacity prediction. The specific capacity of **F1**-**F62** was calculated using the models G2 and G3 using the data set in Table S2 (Scheme S1).[51,52] The following descriptors were calculated using the specific programs: x_n (n = 2, 4, 22, 23) by density functional theory (DFT) using Gaussian 16 under B3LYP functional and 6–311G basis set and x_n (n = 25, 33, 25) using HSPiP version 5.0.03. The others were manually calculated based on the molecular structures. All the calculated capacity was listed in Table S2.

Capacity measurement. The following compounds were selected based on the prediction results and bulk-scale commercial availability. These were used as purchased without further purification: 1,4-dichlorobenzene (**F5**, TCI 99.0 %), 6-methyl-2-pyridinecarboxaldehyde (**F12**, TCI 98.0 %), (*E*)-cinnamyl alcohol (**F21**, TCI 97.0 %), methyl *p*-anisate (**F39**, TCI 99.0 %), formanilide (**F50**, TCI 99.0 %), methyl 3,5-dimethoxybenzoate (**F52**, TCI 99 %), methyl cinnamate (**F58**, TCI 99.0 %), 9,10-dichloroanthracene (**F5-A**, TCI 96.0 %), 1,4-dichloroanthraquinone (**F5-B**, TCI 98.0 %), 1,4,5,8-tetrachloroanthraquinone (**F5-C**, TCI 95.0 %), 1,4-dibromobenzene (**F5-D**, TCI 99.0 %), 1,4-diiodobenzene (**F5-E**, TCI 98.0 %), 1,2,4,5-tetrachlorobenzene (**F5-F**, TCI 99.0 %), 2,6-pyridinedicarboxaldehyde (**F12-A**, TCI 98.0 %), 6-methylpyridine-2-carboxylic acid (**F12-B**, TCI 98.0 %), 2-quinolinecarboxaldehyde (**F12-C**, TCI 97.0 %), pyrrole-2-carboxaldehyde (**F12-D**, TCI 98.0 %), pyrrole-2-carboxylic acid (**F12-E**, TCI 98.0 %). The solid powder of these active materials was mixed with acetylene black carbon (AB, Denka black) and PTFE binder in a mortar without addition of solvents. The weight ratio of the active material, AB, and PTFE was 3:6:1 to ensure the conductivity. The mixture was loaded on a copper mesh (Nilaco) and then pressed by 10 ton for 30 s to prepare the working electrode. As the solvent was not used in the process, the vacuum drying was not performed to avoid sublimation. The electrolyte was ethylene carbonate (EC) and diethyl carbonate (DEC) (1/1 by volume) containing 1 mol dm^{-3} lithium perchlorate ($LiClO_4$) (Tomiyama Pure Chemical). The counter and reference electrodes were metallic lithium (Honjo metal). These electrodes and electrolyte were set in a twin-beaker cell. The galvanostatic charge-discharge measurement was carried out in the range of 0.01–3.0 V vs. Li/Li^+ at 100 mA g^{-1} (Hokuto HJ1001SD8). The capacity of the conductive carbon was corrected using the electrode of AB and PTFE mixed by 9:1 in the weight ratio measured at 50 mA g^{-1}. The method was described with the charge-discharge curves in Fig. S2.

***Ex-situ* FT-IR measurement**. The electrode sample was prepared by mixing the active material (**F5** and **F12**), AB, and PTFE with the weight ratio of 8:1:1 to obtain the sufficient peak intensity of the active material. The electrode was withdrawn after the first discharge (0.01 V vs. Li/Li^+) and subsequent charge (3 V vs. Li/Li^+) cycles at 1 mA g^{-1} and rinsed with DEC and PC (Fuji-Wako 98.0 %). The FT-IR spectra were directly measured using the electrode samples by ATR with the resolution of 4 cm^{-1} and cumulated number 128. The reference sample AB and PTFE with the weight ratio of 9:1 was measured at 8 mA g^{-1}.

Polymerization of F12-D and F12-E. Oxidative polymerization was performed for **F12-D** and **F12-E**. The monomer (1.2 mmol) and ammonium peroxodisulfate (3.6 mmol, APS, Aldrich 98.0 %) were dissolved in 25 cm^3 of 1.2 mol dm^{-3} hydrochloric acid (HCl, Kanto 35-37 %). The solution was stirred at 25 °C for 0.5 h. Then, the monomer (1.2 mmol) was added and stirred at 25 °C for 0.5 h. After addition of the monomer (1.2 mmol) again (total 3.6 mmol), the solution was stirred at 25 °C for 19 h. The resultant precipitate was filtered and rinsed with 1.0 mol dm^{-3} HCl, purified water, and acetone in this order. The sample was vacuum-dried at 80 °C for 20 h. The electrochemical properties were measured by the same method of the monomers.

Structural characterization of pF12-D. The detailed structural characterization was carried out for **pF12-D**. The molecular structures were analysed by KBr method of FT-IR (Jasco FT/IR-4200), Raman spectroscopy (Renishaw, InVia Raman) excited at 532 nm, and XPS (JEOL JPS-9010TR), ^{13}C NMR (JEOL JNM-ECZ400R) with CP/MAS method. The polymerized state and extended conjugated structure were studied by TG (Shimadzu DTG-60) at 10 K min^{-1} under air atmosphere and UV-Vis-NIR with an integrated sphere (Jaso V-670). The crystallinity was characterized by XRD (Bruker, D8 Advance). The composition was analyzed using CHN elemental analysis (Elementar Japan Unicube).

Organic anode active materials in previous works

Table S1. Performances of organic anode active materials in previous works.[15–37,60,68]

Symbol[a]	Compound name or structural characteristics	Current density / mA g^{-1}	Capacity / mA h g^{-1}	Type[b]	Ref.
Low-molecular weight compounds (○: circles)					
A	Dilithium *trans,trans*-muconate	30	549	(i)	15
B	Dilithium thiophene-2,5-dicarboxylate	30	850	(i)	15
C	Dilithium terephthalate	10	1143	(ii)	15
D	Lithium 2,6-Bis(ethoxycarbonyl)-3,7-dioxo-3,7-dihydro-s-indacene-1,5-bis(olate) ($Li_2C_{18}O_8H_{12}\cdot 4H_2O$)	164.3	125	(i)	16
E	Tetralithium salts of 2,5-dihydroxyterephthalicacid ($Li_4C_8H_2O_6$)	24.2	254	(i)	17
F	Dilithium benzenediacrylate	34.9	178	(i)	18
G	Di-lithium 2,6-naphthalene dicarboxylate	235	176	(i)	19
H	2,9-Dimethylquinacridone	100	306	(v)	20
I	Lithium tetrathiafulvalene-dicarboxylate (TTF-Li_2)	88.1	253	(ii)	21
J	Lithium tetrathiafulvalene-tetracarboxylate (TTF-Li_4)	133.6	344	(ii)	21
K	Chelidamic acid	27.5	242	(i)	22
L	Chelidonic acid	10.3	230	(i)	22
M	Itaconic acid ($C_5O_4H_6$)	30	1021	(i)	23
N	Cyclohexanehexanone (C_6O_6)	200	1234	(i)	24
O	5-Formylsalicylic Acid	100	932	(i)	
Polymers (□: squares)					
A	Polyazaacene analogue	100	1231	(iii)	25
B	Benzophenolne-3,3',4,4'-tetracarboxylimide oligomer	42	829	(i)	26
C	Poly(3,3'-bithiophene) (P33DT)	45	1215	(ii)	27
D	Polythiophenyl-triazine-based polymer	100	404	(ii)	28
E	Polytetra(2-thienyl)ethylene	100	973	(ii)	29
F	Poly(benzodithiphene)	20	933	(ii)	60
G	COF containing dehydrobenzoannulene	50	184	(iv)	30
H	COF containing C=C and C=N	100	413	(iv)	31
I	1,3,5-tris(4-aminophenyl) benzene-containing polymer and GO	200	360	(v)	32
J	Hexaazatriphenylene-based polymer	100	405	(iii)	33
K	Polythiohene with C=O groups	20	963	(ii)	68
L	Polycarbonyl-polyimide	100	610	(v)	34
M	Thiophene-diketopyrrolopyrrole-grafted graphene	100	835	(ii)	35
N	COF containing piperazine-terephthalaldehyde	250	556	(iv)	36
O	3,3',4,4'-benzophenonetetracarboxylic dianhydride-based polyimide	25	486	(v)	37
Present work (◇: diamonds)					
	F5	100	424		
	F12	100	279		
	pF12-D	100	871		

[a] The symbols correspond to those in the plots in Fig. 1 and Fig. S1.

[b] Types: (i) Carbonyls. (ii) Thiophene derivatives. (iii) Pyrazine derivatives. (iv) COFs. (v) Others.

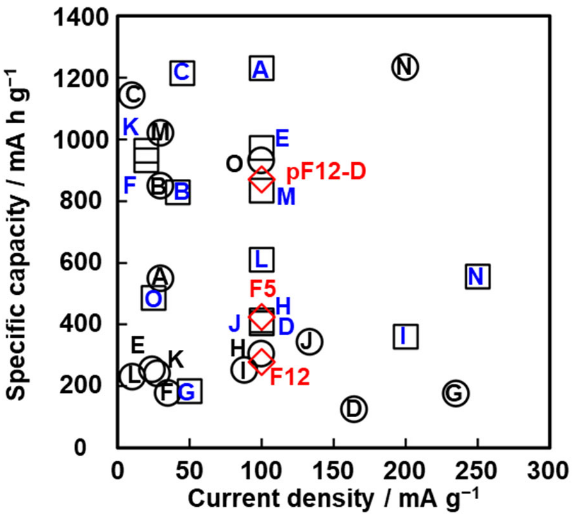

Fig. S1. Relationship between the current density and specific capacity of anode active materials listed in Table S1 and found in the present work (**F5**, **F12**, **pF12-D**).

Table S1 and Fig. S1 summarize the electrochemical performances of organic anode-active materials including the monomers (circles) and polymers (squares) in the previous works. As listed in Table S1, carbonyl compounds (type i) and thiophene derivatives (type ii) are major active materials in the previous works. The new types of the high-performance active materials, such as dichlorobenzene and pyrrole derivatives, have been found in the present work (red colored plots in Fig. S1).

Molecular structures of F1–F62

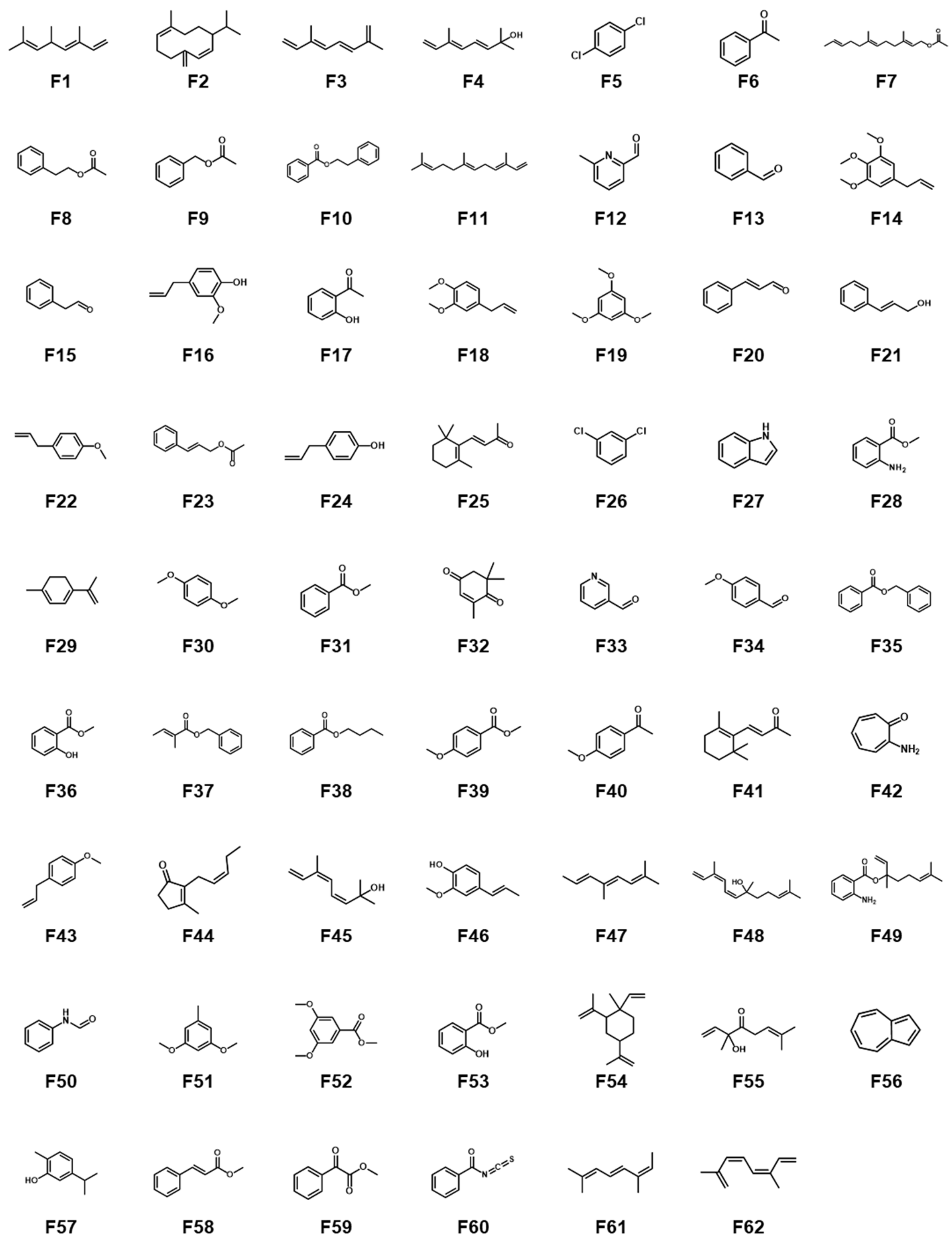

Scheme S1. Molecular structures of **F1–F62** with conjugated moieties as candidates of organic anode active materials extracted from compounds in flower scent.

Predicted capacity of F1–F62

Table S2. Predicted specific capacity of **F1–F62** estimated using the models G2 and G3.

Compounds	x_2	x_4	x_{16}	x_{20}	x_{22}	x_{23}	x_{25}	x_{28}	x_{33}	x_{35}	x_{36}	C_{pred} / mA h g^{-1}	
	/ eV	/ eV	/ g mol^{-1}	/ –	/ –	/ –	/ –	/ D	/ –	/ –	/ –	G2	G3
F1	0.54	1.35	150.27	0	11	1	12.34	0.9667	3.26	0	0	394	269
F2	0.25	1.13	204.36	0	13	1	12.62	0.525	3.44	0	0	233	255
F3	0.73	1.51	134.22	0	11	1	12.30	0.6062	3.45	0	0	486	239
F4	-1.10	1.32	152.24	0	11	1	11.02	1.9123	7.2	0	0	376	175
F5	-0.56	-0.10	147	0	7	4	10.89	0	3.69	0	0.25	65.4	820
F6	0.26	0.98	120.15	1	7	2	8.39	3.4205	4.51	0	0.11	249	423
F7	0.26	0.55	250.38	1	16	1	11.39	2.2499	3.91	0	0.11	160	592
F8	-0.29	1.15	164.2	1	11	3	10.27	2.0495	5.55	0	0.17	291	551
F9	-0.30	1.09	150.18	1	10	3	10.22	1.6913	6.02	0	0.18	296	541
F10	-0.50	-0.23	226.28	1	15	4	10.07	2.1881	3.68	0	0.12	168	555
F11	0.41	1.06	204.36	0	14	1	12.69	0.6344	3.19	0	0	297	282
F12	-1.19	1.01	121.14	1	8	2	6.33	4.2783	7	0	0.22	301	456
F13	-0.71	1.03	106.12	1	7	2	7.84	3.6801	6.22	0	0.13	323	307
F14	0.12	1.12	208.26	0	12	1	9.69	2.7771	5.75	0	0.20	131	550
F15	-0.58	1.06	120.15	1	9	3	7.93	3.0663	5.55	0	0.11	377	305
F16	0.28	0.56	164.2	0	10	1	10.59	2.0849	9.52	0	0.17	215	187
F17	-0.39	0.71	136.15	1	8	2	9.35	4.2585	10.14	0	0.20	225	310
F18	0.03	1.19	178.23	0	10	1	9.39	0.802	5.51	0	0.15	159	356
F19	0.36	1.42	168.19	0	10	0	8.58	3.0879	7.5	0	0.25	222	503
F20	-0.73	0.95	132.16	1	10	3	8.57	4.9576	5.42	0	0.10	379	384
F21	-0.21	1.32	134.18	0	9	2	11.85	1.8693	10.77	0	0.10	337	-36
F22	0.01	1.20	148.21	0	10	1	10.00	1.4136	4.82	0	0.09	321	289
F23	-0.37	1.04	176.22	1	11	3	10.71	2.3495	5.47	0	0.15	225	555
F24	-0.04	0.73	134.18	0	9	2	11.14	1.7189	9.5	0	0.10	312	20
F25	0.41	1.07	192.3	1	12	1	10.58	5.4118	3.16	0	0.07	218	605
F26	-1.12	0.41	147	0	7	3	11.44	2.3511	2.62	0	0.25	93	1010
F27	0.63	1.61	117.15	0	8	1	11.03	2.152	7.42	0	0.11	374	223
F28	0.18	1.33	151.17	1	9	1	8.90	3.5599	9.18	0	0.27	239	540
F29	0.82	1.46	134.22	0	10	1	12.09	1.0533	4.36	0	0	416	172
F30	0.45	1.34	138.17	0	9	1	8.66	2.963	6.86	0	0.20	307	414
F31	-0.47	1.18	136.15	1	9	2	7.81	1.9596	4.95	0	0.20	302	555
F32	-0.72	1.32	152.19	2	10	2	5.44	1.0034	4.18	0	0.18	277	475
F33	-1.40	0.90	107.11	1	7	2	7.07	4.4178	8.25	0	0.25	309	480
F34	-0.69	0.94	136.15	1	10	2	7.26	4.1633	7.43	0	0.20	356	407
F35	-0.54	-0.24	212.25	1	14	4	9.87	1.9925	3.9	0	0.13	174	540
F36	-0.28	1.15	152.15	1	9	2	8.96	3.3559	10.16	0	0.27	221	459
F37	-0.34	1.01	190.24	1	11	3	10.90	1.8779	5.02	0	0.14	150	554
F38	-0.45	1.16	178.23	1	11	2	8.79	2.1348	4	0	0.15	215	559
F39	-0.48	1.38	166.18	1	11	2	7.10	1.8526	6.04	0	0.25	279	566
F40	-0.56	0.97	150.18	1	10	2	7.56	5.2549	5.86	0	0.18	284	533
F41	0.47	1.20	192.3	1	11	1	10.58	3.7635	3.16	0	0.07	157	548
F42	-1.50	1.12	121.14	1	6	2	8.13	3.8896	8.43	0	0.22	181	427
F43	0.03	1.18	148.21	0	10	1	10.00	1.7046	4.82	0	0.09	321	299
F44	0.39	1.17	164.25	1	11	1	9.59	4.3482	4.73	0	0.08	300	425
F45	0.47	1.51	152.24	0	11	1	11.02	1.4107	7.2	0	0.09	384	157
F46	-0.02	1.22	164.2	0	10	2	10.98	1.5782	9.79	0	0.17	236	169
F47	1.15	1.46	136.24	0	10	1	12.44	0.3215	3.54	0	0	407	230
F48	0.45	0.86	220.36	0	14	1	12.06	1.2147	5.72	0	0.06	201	243
F49	0.02	0.49	273.38	1	17	1	10.44	3.5896	4.63	0	0.15	97	639
F50	-0.64	0.91	121.14	1	8	2	9.09	3.7939	10.83	0	0.11	311	-21
F51	0.36	1.42	152.19	0	9	0	9.06	1.5372	6.28	0	0.18	243	381
F52	0.09	1.33	196.2	1	12	1	7.32	1.3086	6.67	0	0.29	191	609
F53	-0.28	1.15	152.15	1	9	2	8.96	3.3559	10.16	0	0.27	221	459
F54	0.45	0.98	204.36	0	13	0	12.94	1.0373	1.46	0	0	235	445
F55	0.10	0.63	168.24	1	11	1	9.27	2.6891	7.64	0	0.17	256	355
F56	-1.21	1.57	128.17	0	8	2	11.68	1.204	6.74	0	0	311	-31
F57	0.16	1.15	150.22	0	9	1	10.70	1.5423	7.2	0	0.09	246	145
F58	-0.56	1.08	162.19	1	10	2	10.64	3.0279	5.7	0	0.17	240	592
F59	-0.91	0.53	164.16	2	11	3	7.88	4.7222	6.62	0	0.25	255	733
F60	-1.13	-0.66	163.19	1	10	4	7.94	4.3298	7.62	0	0.36	143	890
F61	-1.16	1.42	136.24	0	10	1	12.44	0.4417	3.54	0	0	406	234
F62	0.01	1.41	134.22	0	10	1	12.30	0.5261	3.45	0	0	415	237

The compounds colored by blue, red, and yellow were extracted based on the prediction results using the models G2, G3, and both, respectively.

Charge-discharge curves of the candidates

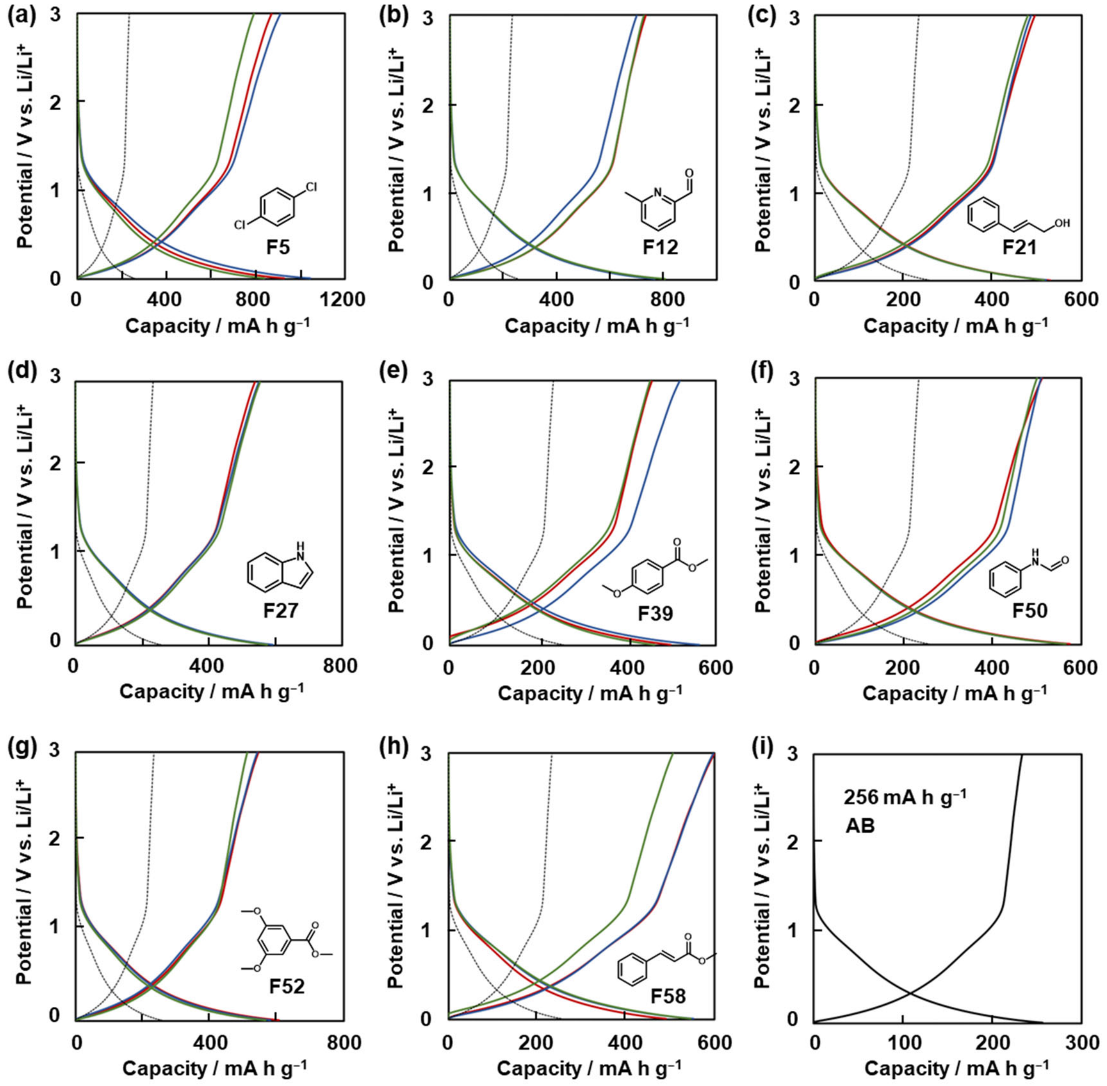

Fig. S2. Charge-discharge curves of **F5** (a), **F12** (b), **F21** (c), **F27** (d), **F39** (e), **F50** (f), **F52** (g), **F58** (h), and reference acetylene black carbon (AB, 50 mA g^{-1}) (i) at the second cycle at 100 mA g^{-1}. The colored and black dashed curves correspond to the three different samples of the targeted compounds (*N* = 3) and AB, respectively. The red, blue, and green curves correspond to the samples 1, 2, and 3 in Table S3.

Table S3. Reproducibility of the specific capacity.

Sample ($N = 3$)	**F5**	**F12**	**F21**	**F27**	**F39**	**F50**	**F52**	**F58**
Discharge capacity at 2nd cycle / mA h g^{-1}								
1	413.7	289.0	0	67.7	0	61.5	93.1	0
2	532.4	254.6	0	79.1	49.9	45.0	68.1	40.1
3	325.9	293.0	0	62.8	0	52.4	53.3	56.9
Average	424.0	278.9	0	69.9	16.6	53.0	71.5	13.4
Capacity retention rate after 10 cycles / %								
1	91.6	91.6	N. A.	165.6	N. A.	128.5	109.6	N. A.
2	86.3	81.3	N. A.	95.4	133.2	92.1	111.8	186.9
3	94.5	86.1	N. A.	136.1	N. A.	88.5	92.6	107.5
Average	90.8	86.3	N. A.	132.4	133.2	103.0	104.6	147.2

The measured capacity was corrected to exclude the capacity of AB. The actual capacity was calculated using (Eq. S1), where the actual specific capacity of the target compound is C mA h g^{-1}, the measured specific capacity is C_{meas} mA h g^{-1} at 100 mA g^{-1}, the weight of the active material is W_{a} mg, the specific capacity of AB is C_{AB} mA h g^{-1} at 50 mA g^{-1}, and weight of AB is W_{AB} mg. As the weight ratio of the active material, AB, and binder was 3:6:1, the specific capacity of the active material and AB measured at the different current density was used for the correction.

$$C = (C_{\mathrm{meas}} \times W_{\mathrm{a}} - C_{\mathrm{AB}} \times W_{\mathrm{AB}}) / W_{\mathrm{a}} \ldots \text{(Eq. S1)}$$

As shown in Table S3, **F5**, **F12**, **F27**, **F50**, and **F52** showed the specific capacity for the three samples. In these samples, the red-colored highest values were used in the main text. In contrast, **F21**, **F39**, and **F58** had the lower capacity

Charge-discharge curves at the first cycle

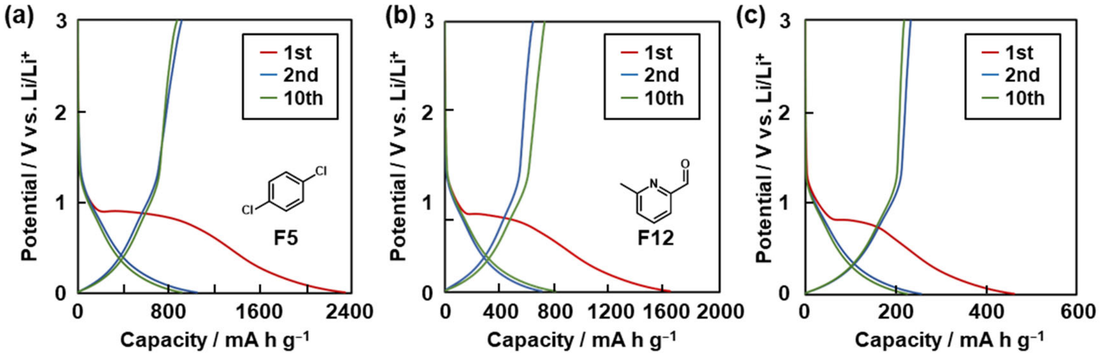

Fig. S3. Representative charge-discharge curves of **F5** (a), **F12** (b), and reference AB (c) at the 1st (red), 2nd (blue), and 10th (green) cycles at 100 mA g^{-1}.

Compared with the following cycles, the first discharge cycle had the large irreversible capacity originating from formation of SEI (red discharge curves in Fig. S3).

CV curves

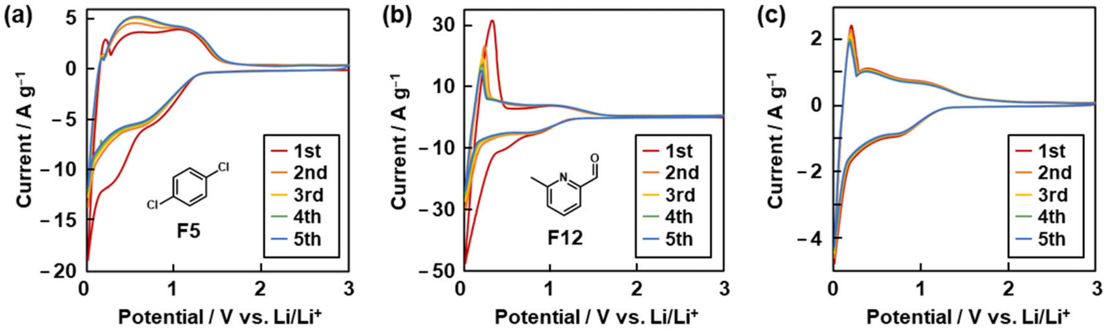

Fig. S4. CV curves of **F5** (a), **F12** (b), and reference AB (c) for the initial five cycles at 5 mV s^{-1}.

Based on the CV curves, **F5** and **F12** had the specific capacity 512 and 1396 F g^{-1} at the second cycle after the subtraction of that originating from AB, respectively. The first cycle showed the larger current originating from the SEI formation (red curves in Fig. S4). After the second cycles, the reversible redox reactions were observed in the potential range lower than 1.5 V vs. Li/Li^+.

Ex-situ FT-IR of reference AB

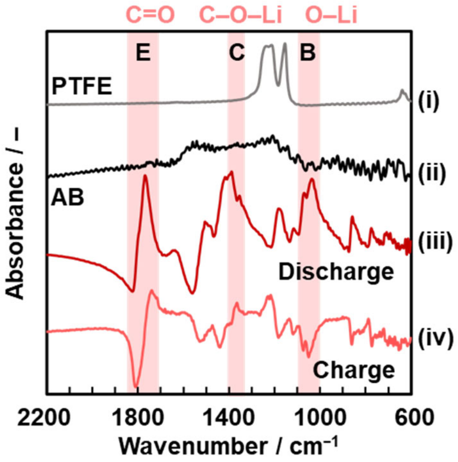

Fig. S5. FT-IR spectra of PTFE (i) and pristine AB (ii) and *Ex-situ* FT-IR spectra of AB after the 1st discharge (iii) and subsequent charge (iv) cycles.

The strong absorption bands B, C, and E correspond to O–Li, C–O–Li, and C=O bonds (Fig. S5).[65] These absorption bands were intensified after the discharge cycle and then weakened after the charge cycle. These band were observed for the electrode only consisting of AB, indicating the SEI formation originating from decomposition of the electrolyte. In addition to these absorptions originating from AB, C=C stretching vibration in benzene ring was observed around 1500 cm^{-1} after the discharge cycles of **F5** and **F12**.

Charge-discharge curves of F5 analogues

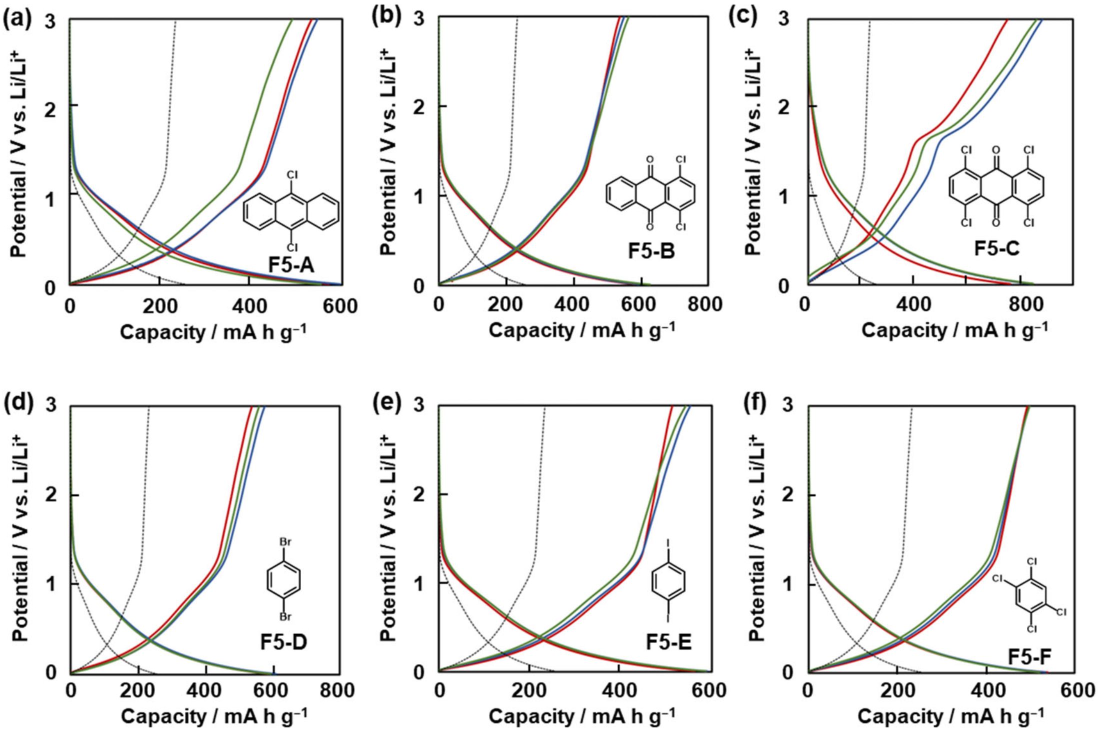

Fig. S6. Charge-discharge curves of **F5-A** (a), **F5-B** (b), **F5-C** (c), **F5-D** (d), **F5-E** (e), **F5-F** (f) at the second cycle at 100 mA g^{-1}. The colored and black dashed curves correspond to the three different samples of the targeted compounds ($N = 3$) and reference AB, respectively. The red, blue, and green curves correspond to the samples 1, 2, and 3 in Table S4, respectively.

Table S4. Reproducibility of the specific capacity.

Sample ($N = 3$)	**F5-A**	**F5-B**	**F5-C**	**F5-D**	**F5-E**	**F5-F**
Discharge capacity at 2nd cycle / mA h g^{-1}						
1	58.5	69.9	250.8	75.3	69.7	26.7
2	82.3	81.5	328.3	97.7	95.4	22.6
3	40.5	114.7	337.7	82.7	112.6	8.5
Average	60.5	88.7	305.6	85.2	92.6	19.3
Capacity retention rate after 10 cycles / %						
1	108.1	132.2	53.9	106.4	69.7	0
2	96.2	136.4	77.5	77.6	95.4	104.0
3	19.6	67.6	76.9	84.9	112.6	316.8
Average	74.6	112.1	69.4	89.6	92.6	140.3

In these samples, the red-colored highest values were used in the main text.

DFT calculation of F5 analogues

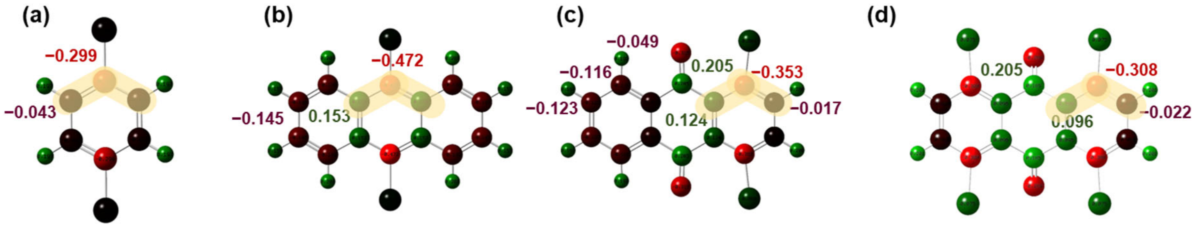

Fig. S7. Charge-density distribution of **F5** (a), **F5-A** (b), **F5-B** (c), and **F5-C** (d) based on DFT calculation. The values of charge density were added only for carbons. The values for the equivalent sites were omitted for clarity.

Here the charge negativity of carbons in dichlorobenzene unit was compared for these four compounds (yellow shadows in Fig. S7). The values indicate the charge localization for **F5-A** and **F5-B** with low specific capacity (Fig. S7b,c). On the other hand, the charge density is delocalized for **F5** and **F5-C** with the higher specific capacity (Fig. S7a,d). The difference can have relevance with the specific capacity, *i.e.* the reactivity with Li^+. However, the structure-reactivity relationship of conjugated molecules as organic anode active materials is still unclear. The comprehensive calculation study facilitates understanding the reactivity.

Charge-discharge curves of F12 analogues

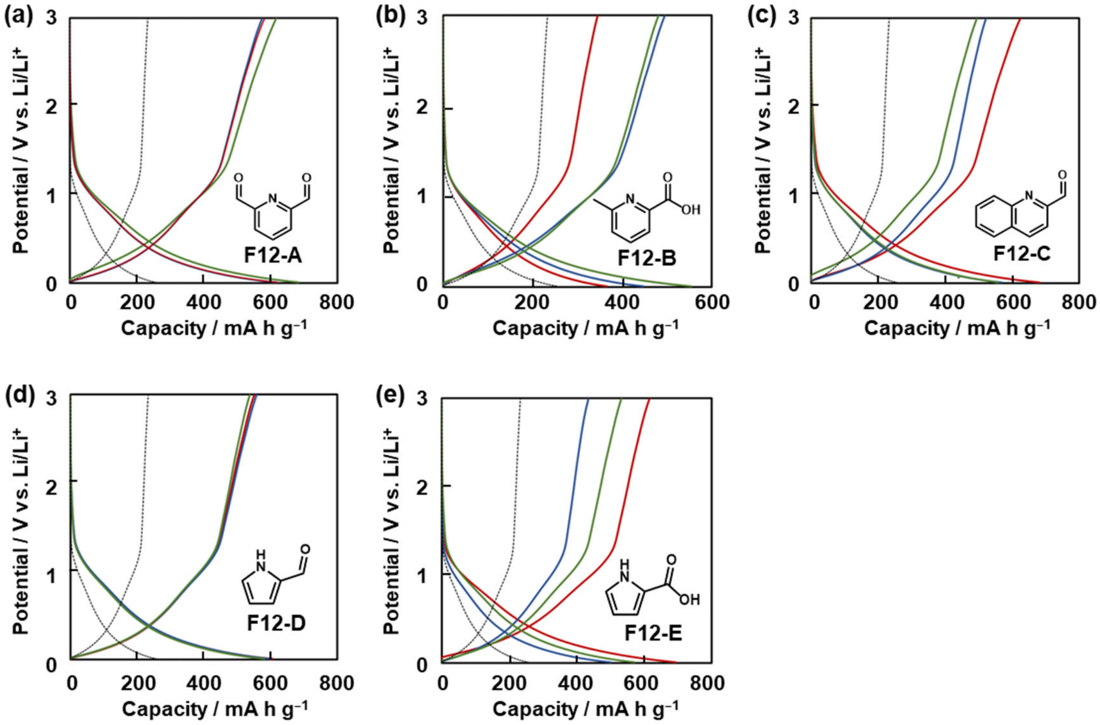

Fig. S8. Charge-discharge curves of **F12-A** (a), **F12-B** (b), **F12-C** (c), **F12-D** (d), **F12-E** (e) at the second cycle at 100 mA g^{-1}. The colored and black dashed curves correspond to the three different samples of the targeted compounds ($N = 3$) and reference AB, respectively.

Table S5. Reproducibility of the specific capacity.

Sample ($N = 3$)	**F12-A**	**F12-B**	**F12-C**	**F12-D**	**F12-E**
Discharge capacity at 2nd cycle / mA h g^{-1}					
1	108.6	0	169.5	92.7	180.5
2	105.2	0	57.1	87.3	59.4
3	171.0	41.7	45.9	69.9	0
Average	128.3	13.9	90.8	83.3	80.0
Capacity retention rate after 10 cycles / %					
1	97.5	N. A.	114.5	99.1	83.8
2	86.3	N. A.	97.1	109.0	69.1
3	84.5	52.0	37.7	92.1	N. A.
Average	89.4	52.0	83.1	100.1	76.5

In these samples, the red-colored highest values were used in the main text.

Relationship between predicted and measured capacity

Table S6. Summary of the predicted and measured capacity.

mA h g^{-1}	**F5**	**F5-A**	**F5-B**	**F5-C**	**F5-D**	**F5-E**	**F5-F**
[a] $C_{\mathrm{pred,G2}}$	65.4	−209	−279	−543	−431	[c] N. A.	−197
[a] $C_{\mathrm{pred,G3}}$	820	129	−102	109	−77	[c] N. A.	274
[b] C_{meas}	424	60.5	88.7	306	85.2	92.6	19.3
mA h g^{-1}	**F12**	**F12-A**	**F12-B**	**F12-C**	**F12-D**	**F12-E**	
[a] $C_{\mathrm{pred,G2}}$	301	−119	390	256	423	494	
[a] $C_{\mathrm{pred,G3}}$	456	−331	279	273	798	457	
[b] C_{meas}	278	128	13.9	90.8	83.3	80.0	

[a] $C_{\mathrm{pred,G2}}$, $C_{\mathrm{pred,G3}}$: Predicted capacity based on the models G2 and G3, respectively.

[b] C_{meas}: Measured capacity collected from the average values in Tables S3–S5.

[c] C_{pred} was not calculated because DFT calculation was failed.

Table S6 summarizes the predicted and measured capacity to validate the prediction accuracy of the models G2 and G3.

Charge-discharge curves of pF12-D and pF12-E

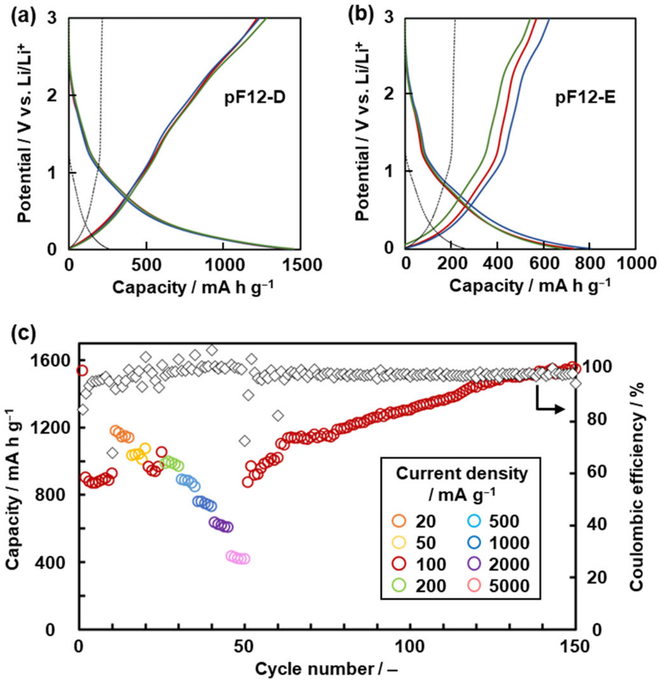

Fig. S9. Charge-discharge curves of **pF12-D** (a) and **pF12-E** (b) at the second cycle at 100 mA g^{-1}. The colored and black dashed curves correspond to the three different samples of the targeted compounds ($N = 3$) and reference AB, respectively. (c) Specific capacity (left axis) and Coulombic efficiency (right axis) of **pF12-D** with changes in the current density for each five cycle from 20–5000 mA g^{-1}.

The specific capacity of **pF12-D** and **pF12-E** had the reproducibility (Fig. S9a,b). The rate and cycle stability were studied by changes in the current density (Fig. S9c). The specific capacity was decreased with increasing the current density in the initial 50 cycles. The capacity decrease is ascribed to lack of the conductivity. After that, the long-term cycle stability was measured at 100 mA g^{-1}. The specific capacity slightly increased with increasing the cycle number. Such increase in the specific capacity was observed in our previous work.[63] The Coulombic efficiency is about 100 % for all the cycles. The structure of active materials is gradually optimized with formation of SEI and improvement of affinity to electrolyte.

Table S7. Reproducibility of the specific capacity.

Sample ($N = 3$)	**pF12-D**	**pF12-E**
Discharge capacity at 2nd cycle / mA h g^{-1}		
1	897.2	208.4
2	911.0	284.9
3	934.2	160.1
Average	914.1	217.8
Capacity retention rate after 10 cycles / %		
1	104.1	70.8
2	109.3	80.2
3	104.7	114.9
Average	106.0	88.6

In these samples, the red-colored highest values were used in the main text.

Additional structural analyses of pF12-D

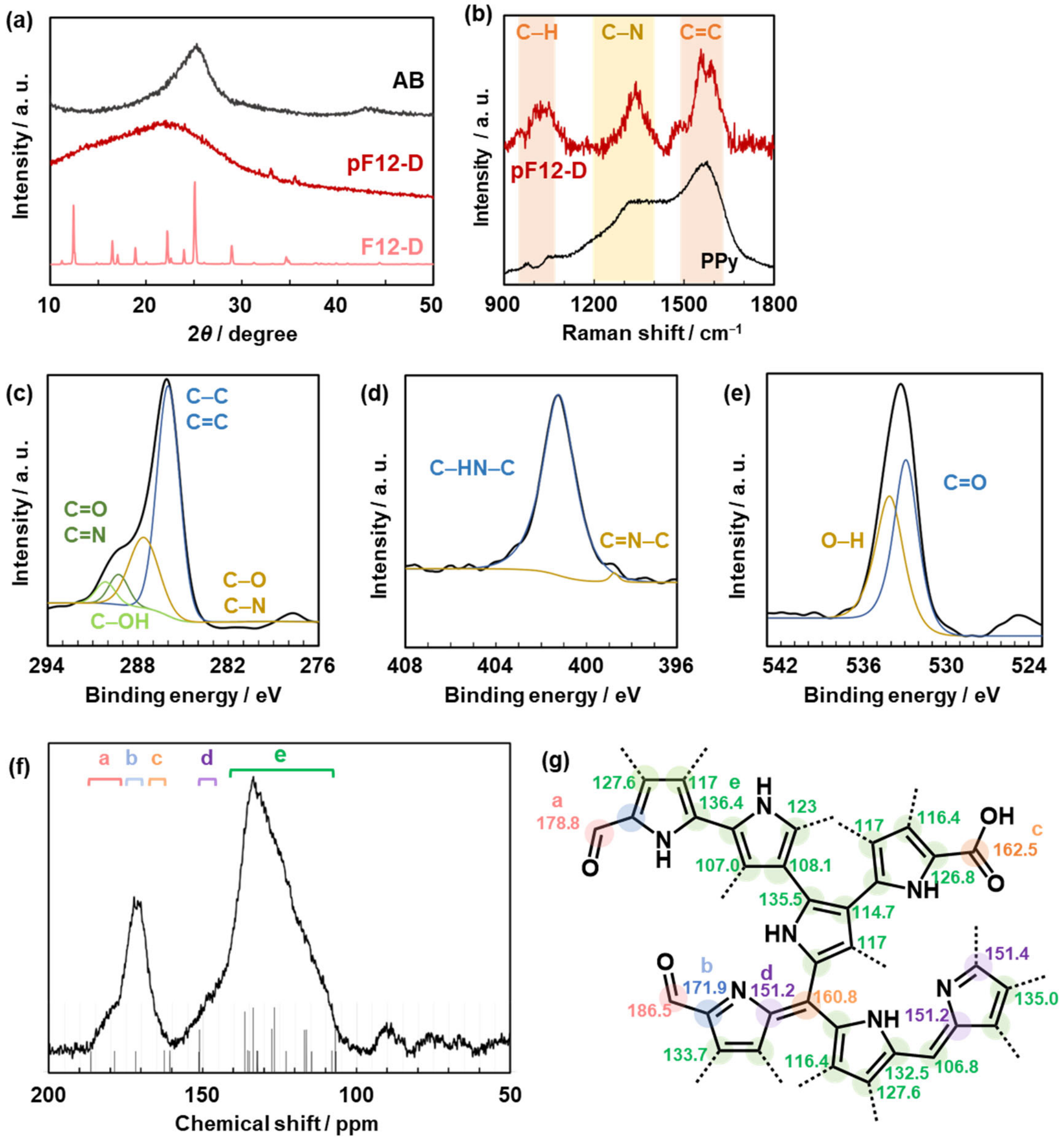

Fig. S10. Additional structural analyses of **pF12-D**. (a) XRD patterns of **F12-D**, **pF12-D**, and reference AB. (b) Raman spectra of **pF12-D** and reference PPy. (c–e) C1s (c), N1s (d), and O1s (e) XPS profiles of **pF12-D**. (f,g) ^{13}C solid-state NMR spectrum of **pF12-D** (f) and its simulation results (g).

Table S8. Elemental analysis of **pF12-D**.

wt %	C	H	N	Others (O, Cl)[c]	Cl[d]
[a] Linear	64.52	3.23	15.08	17.20 (O)	N. A.
Measured	52.48 ± 0.05	3.82 ± 0.01	13.61 ± 0.01	27.79 ± 0.06	2.81±0.04
[b] Calculated	53.06	4.40	14.18	28.36	2.31

[a] Calculated values of the linearly polymerized **F12-D**.

[b] Calculated value of the estimated structure in Fig. 6f.

[c] Measured using CHN elemental analysis.

[d] Measured using elemental analysis for halogens.

The XRD patterns indicate the amorphous nature of **pF12-D** (Fig. S10a). The sharpened peaks of the **F12-D** monomer disappeared. The hallo broader than that of AB was observed after the polymerization. This is characteristic of the amorphous CPN.[67] In XPS, the peak separation indicates that the profiles contained all the peaks originating from the bonds in the estimated structure in Fig. 6f (Fig. S10c–e). ^{13}C NMR showed the spectrum with the two broadened peaks (Fig. S10f). Based on the estimated structure (Fig. 6g), the simulated peaks are calculated and added in the bottom of the spectrum in Fig. S10f. The observed spectrum is regarded as the sum of the simulated peaks.

In Table S8, the proportion of the others was the measured values of the elements other than C, H, and N. In the present work, the others correspond to proportion of O and Cl (note c). The proportion of Cl was measured using another elemental analysis for halogens (note d). The measured composition was different from that of the linearly linked **F12-D**.